Research Square

Preprints are preliminary reports that have not undergone peer review.
They should not be considered conclusive, used to inform clinical practice,
or referenced by the media as validated information.

Chemical Interactions between Palladium and UCO Nuclear Fuel Kernel

Jana Howard

jana.howard@inl.gov

Idaho National Laboratory

Kaustubh Bawane

Idaho National Laboratory

Steven Cavazos

The University of Texas at San Antonio

Anshul Kamboj

Idaho National Laboratory

Jahangir Khan Lodhi

Idaho National Laboratory

Guang Yang

Idaho National Laboratory

Ching-Heng Shiau

Critical Materials and Energy Systems Innovation Center

Patrick Warren

The University of Texas at San Antonio

Elizabeth Sooby

The University of Texas at San Antonio

Tiankai Yao

Idaho National Laboratory

Haiyan Zhao

University of Idaho

Article

Keywords: UCO, TRISO fuel, palladium, fission products, chemical interactions

Posted Date: November 11th, 2026

DOI: https://doi.org/10.21203/rs.3.rs-10913713/v1

License: This work is licensed under a Creative Commons Attribution 4.0 International License.
Read Full License

Additional Declarations: No competing interests reported.

Chemical Interactions between Palladium and UCO Nuclear Fuel Kernel

Jana Cu Howard [a,b,*], Kaustubh Bawane [a,*], Steven Cavazos [c], Anshul Kamboj [a], Jahangir Khan Lodhi [a], Guang Yang [a], Ching-Heng Shiau [d], Patrick Warren [c], Elizabeth Sooby [c], Tiankai Yao [e], Haiyan Zhao [e,f,*]

[a] Nuclear Materials Performance Division, Idaho National Laboratory, Idaho Falls, ID, 83415, USA

[b] Department of Natural Resources, University of Idaho, Idaho Falls, ID, 83402, USA

[c] Department of Physics and Astronomy, University of Texas at San Antonio, San Antonio, TX, 78249, USA

[d] Critical Materials and Energy Systems Innovation Center (CMESIC), Idaho Falls, ID, 83401, USA

[e] Fuel Development, Performance, and Qualification Department, Idaho National Laboratory, Idaho Falls, ID, 83415, USA

[f] Department of Chemical and Biological Engineering, University of Idaho, Idaho Falls, ID, 83402, USA

*Corresponding authors: jana.howard@inl.gov, kaustubh.bawane@inl.gov, haiyanz@uidaho.edu

Abstract

Tri-structural Isotropic (TRISO) particle fuel is an advanced coated-particle system engineered to limit fission-product release through its multilayer containment architecture, yet uncertainties

remain on how fission product–fuel chemical interactions influence fuel microstructure and mechanical performance. In this study, a palladium (Pd) and UCO fuel kernel diffusion couple was annealed at 1100°C for 100 hours enabling direct observation of previously uncharacterized diffusion behavior and chemical interactions between fission product and fuel matrix. This study, through Scanning Transmission Electron Microscopy – Energy-Dispersive X-ray Spectroscopy (STEM-EDS) mapping and selected area electron diffraction (SAED) revealed a degradation mechanism of UCO under high temperature annealing and Pd diffusion. The annealed UCO showed the emergence of carbon discontinuous precipitates along UC grain boundaries and U_2C_3 string precipitates within UC grains. The interfacial region between UCO and Pd mainly showed reaction products like UPd_3 and carbon. Nanoindentation technique revealed a decrease in average hardness in regions where UPd_3 and porous areas were present.

Keywords: UCO, TRISO fuel, palladium, fission products, chemical interactions

1. Introduction

The production of nuclear energy is directly affected by the composition of the fuel and its design. Nuclear fuels are commonly fabricated as uranium-based pellets housed within rods or pins, but alternative configurations also exist; one notable example is the Tri-structural Isotropic (TRISO) fuel architecture[1–3]. TRISO particles consist of different layers: a uranium-based fuel kernel in the center, a porous carbon buffer, an inner pyrolytic carbon (IPyC), silicon carbide (SiC), and finally an outer pyrolytic carbon (OPyC)[4,5]. The SiC layer functions as the primary fission-product (FP) barrier, providing exceptional mechanical strength, thermal stability, and chemical inertness under reactor operating conditions. Surrounding the fuel kernel, the IPyC

accommodates kernel swelling and protects the kernel during fabrication, while the OPyC preserves overall structural integrity and helps distribute mechanical stresses throughout the coating system. Between these layers, the porous carbon buffer absorbs fission gases and provides additional margin for kernel expansion, thereby reducing stress transmitted to the SiC layer[1–5].

TRISO fuel can withstand high temperatures due to its encapsulated design which enables it to maintain structural integrity while containing FPs[3,6,7]. TRISO's encapsulated design allows compatibility with numerous fuel kernel materials[3,8]. Originally, carbide kernels were favored due to their robust performance in high temperature conditions, but it was found that it readily oxidizes and chemically reacts with surrounding SiC layers[5]. Oxide kernels began gaining traction due to better chemical stability[7,8]. It was later found that oxide kernels cause a release of oxygen forming carbon monoxide (CO) with the carbon layers encapsulating the kernel[5]. This causes an increase in internal pressure causing a failure of the encapsulation[9,10]. Due to this, a fuel kernel consisting of oxides (UO_2) and carbides (UC), such as UCO, was introduced where UC serves as an oxygen trap to mitigate the release of CO gases[9–12]. As uranium splits, the UO_2 phase releases oxygen. If not trapped, this oxygen reacts with the carbon buffer layer and continues to build up pressure inside the kernel. The UC acts as an oxygen trap by preferentially forming stable actinide oxides rather than liberating oxygen that forms CO gas at the buffer layer[10–13].

As nuclear fuel experiences high temperature conditions, FPs tend to mobilize and be released across different components of the fuel assembly including the fuel kernel via bulk diffusion process traveling along grain boundaries and across grains. The production of FPs in a fuel system introduces an array of chemical and physical interactions such as formation of gaseous FPs, metallic alloying and precipitation, and gas bubble formation[9,14–16]. This study focuses on Pd, one of the high-yield metallic FPs[16–18]. Pd is known to form various phases and, due to its limited

solubility, it often presents as metallic inclusions within irradiated oxide fuel[16]. Pd-fuel interactions are well-documented across different reactor systems. For instance, in high-temperature gas-cooled reactors, Pd has been observed to react with SiC layers, leading to the formation of corrosion nodules[19–21]. Pd also plays a role in facilitating the diffusion of other FPs through a corrosion-driven failure mechanism. This occurs as chemical reactions between Pd and SiC initiated at cracks, resulting in Pd-rich precipitates along SiC grain boundaries and smaller precipitates within SiC grains[17,22]. Pd has also been identified as an effective agent for binding other FPs, aiding in their immobilization and preventing potential corrosion at the fuel-cladding interface[20,23]. Finally, in U-10Zr fuel systems, Pd has been found to induce carbonization and decarbonization in certain regions, leading to the development of new microstructures[10].

Evidently, Pd as an FP in nuclear fuel, can undergo chemical reactions, form intermetallic precipitates, and drive the development of new microstructures within the fuel matrix. The formation of these Pd precipitates alters key fuel properties, including melt point and oxidation properties, thereby influencing overall fuel performance[14,24,25]. Due to this, it is imperative to further the knowledge of these fuel-to-FP interactions. In this study, we fill the gap in understanding how fuel degradation serves as nucleation sites for FP precipitates. This study provides detailed microscopy evidence of UC degradation that led to the presence of grain boundary carbon discontinuous precipitates and intragranular U_2C_3 strings, which serve as Pd precipitate nucleation sites resulting in new microstructures.

2. Results and Discussion

2.1. Thermally driven changes in pristine UCO

Observations were made on the microstructural changes that occurred after subjecting the UCO fuel kernel to Pd foil at 1100 °C for 100 hours. Figure 1a shows scanning electron microscope (SEM) image, STEM (Scanning Transmission Electron Microscope) - High-Angle Annular Dark Field (HAADF) images, and STEM-EDS (Energy Dispersive X-ray Spectroscopy) mapping of pristine UCO with distinct UC and UO_2 grains. Pristine UCO highlights the grain boundary before any degradation or phase growth. In contrast, STEM-EDS mapping of the reacted UCO kernel in Figure 1b identifies UC and UO_2 grains, accompanied by carbon discontinuous precipitates localized at grain boundaries. Similar discontinuous precipitate formation was previously reported in some metallic fuels like U10Mo alloy[23,25]. The discontinuous precipitates were described as alternating lamellar structures of molybdenum (Mo) enriched U-Mo and α-U[23]. Submicron UO_2 grains (<1 μm) were observed embedded within UC matrix grains. The intragranular elongated precipitates within UC grains were found to be carbon rich. Selected area electron diffraction (SAED) patterns in Figure 1c validated the cubic fluorite structure of UO_2 and the cubic rock salt structure of UC. Althaus et al. also previously identified the discontinuous precipitates as "colony" precipitates common in uranium carbide systems[26]. These "colonies" were described as forming an interconnected fine network structure at the grain boundaries[23,26,27]. The UC phases within this UCO fuel system remained consistent with prior reports, exhibiting UC "colonies" or discontinuous precipitates at the grain boundaries even in the presence of UO_2. Similar to the previously mentioned U10Mo, which displayed discontinuous precipitates with alternating UMo and U structures, it was observed in the Pd exposed UCO sample that the discontinuous precipitate

consisted of alternating UC and C lamellar structures. This is depicted in Figure 1b and supplemental Figures S2 and S3. Studies indicate that the formation of precipitates, such as U_2C_3, is influenced by annealing temperature, heating duration, and the U-C atomic ratio[24,28,29]. The ternary phase diagram in Figure 5a supports the presence of C and U_2C_3 phases during annealing at 1100ºC. Moreover, STEM-EDS image in Figure 1b revealed carbon-rich intragranular elongated precipitates within the UC matrix. These observations align closely with earlier findings which noted that U_2C_3 typically appears as intragranular strings traversing the UC grains[30,31]. Figure S2 in the supplementary information shows these intragranular elongated U_2C_3 precipitates at high magnification.

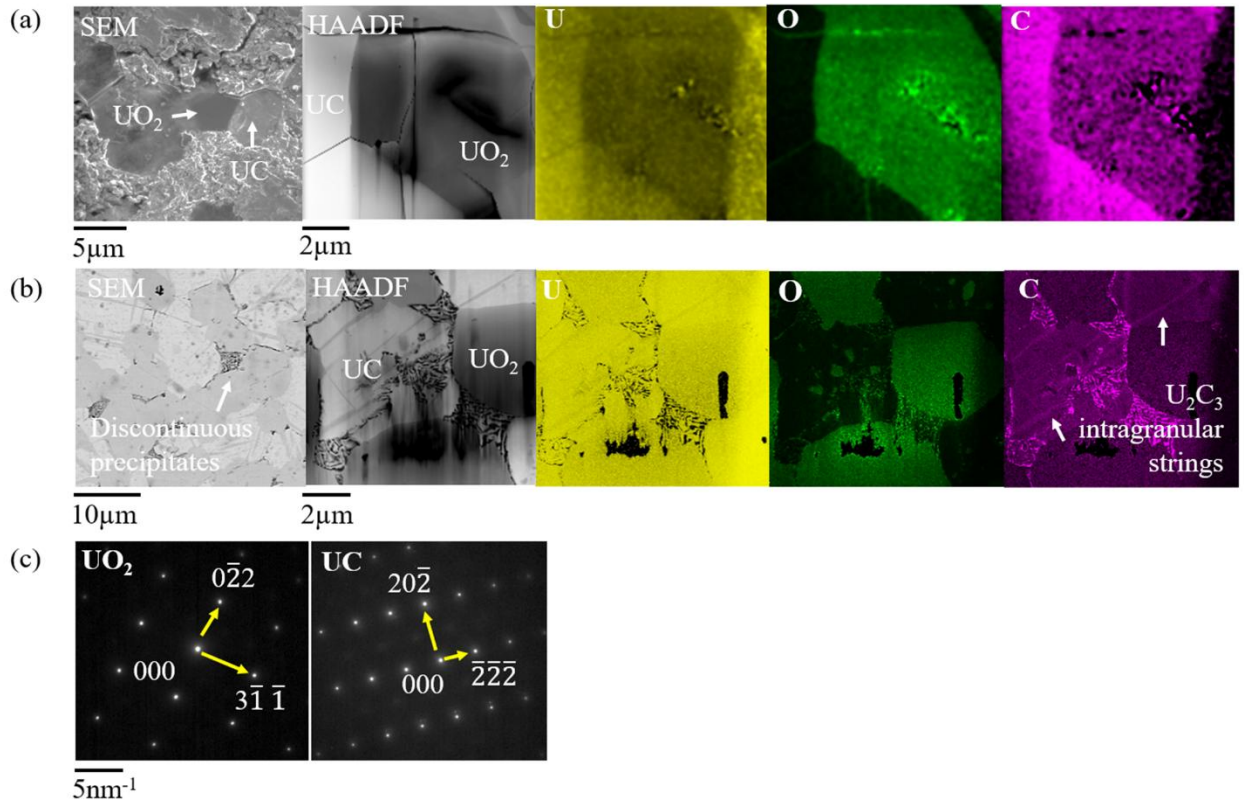


Figure 1. STEM-EDS and SAED analysis of pristine and annealed UCO. (a) SEM, HAADF image, and weight percent STEM-EDS maps of pristine UCO confirming presence of UC and

UO_2. After annealing, grain boundary carbon discontinuous precipitates and intragranular U_2C_3 string precipitates formed: (b) SEM, HAADF image, and STEM-EDS mapping of annealed UCO region, (c) SAED patterns for UC and UO_2 at the annealed UCO revealing cubic rock salt and cubic fluorite structure respectively.

2.2. Chemical interactions between UCO and Pd

Figure 2 presents surface SEM images of the Pd interaction zone including region 1 at the interface, region 2 with lamellar structure, and region 3 with equiaxed grains. Overall, the grains in the Pd interaction zone exhibit irregular shapes and sizes. Furthermore, Figure 2b also exhibits a more porous morphology in the interaction zone compared with the pristine and annealed UCO. 'Interface' region is where the UCO kernel and Pd bar make contact. STEM-EDS analysis of Zone 1 lift-out at the interface is shown in Figure 3. A high concentration of U and Pd distributed throughout the region is observed while UC and UO_2 phases were not prominent. As shown in Figure 3a, carbon rich precipitates were also observed dispersed across the lamella. The bright yellow feature in uranium "U" EDS map is likely UC leftover from Pd reaction. SAED patterns from two points on either side of the interface confirmed the presence of hexagonal UPd_3. The presence of UPd_3 in this region suggests higher concentration of diffused Pd and spontaneous formation of UPd_3 across the region, also supported by negative Gibbs free energies as shown in Figure 6.

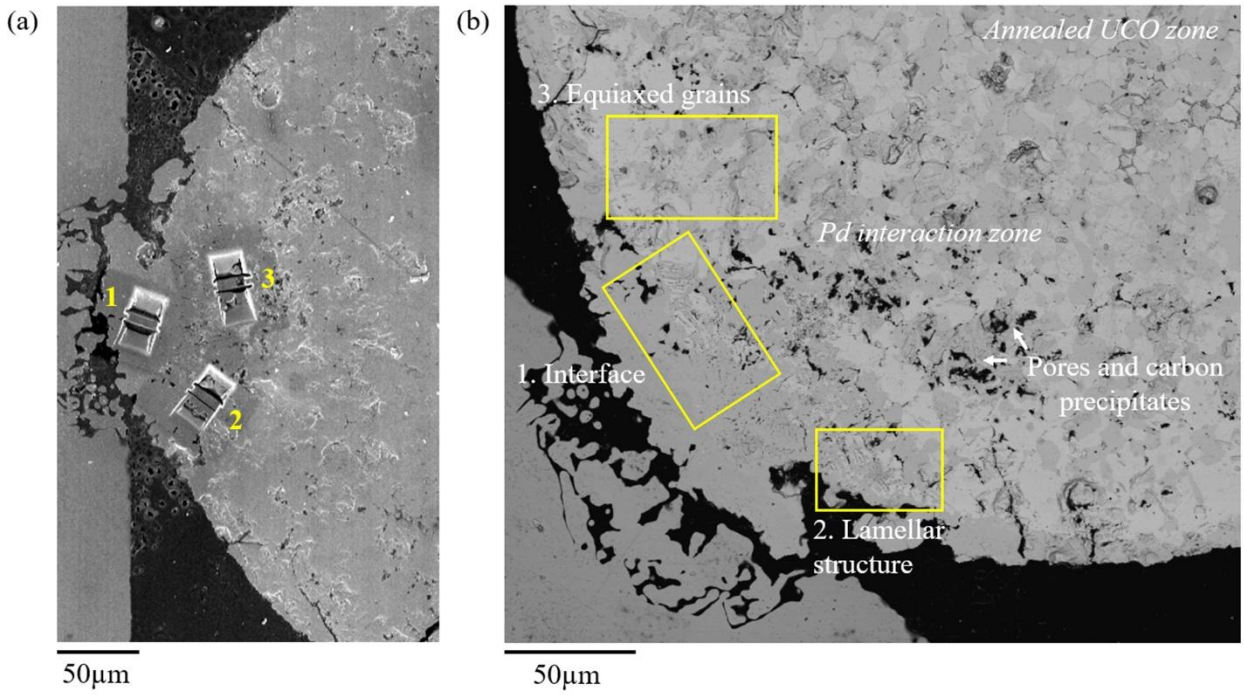


Figure 2. SEM image showing lift-out sites at the Pd interaction zone: (a) SEM image of lift out locations (b) SEM image depicting Pd interaction zone: location 1 is on interface between Pd bar and UCO kernel, location 2 is on the interaction zone over a lamellar structure, location 3 is on the interaction zone over the equiaxed region.

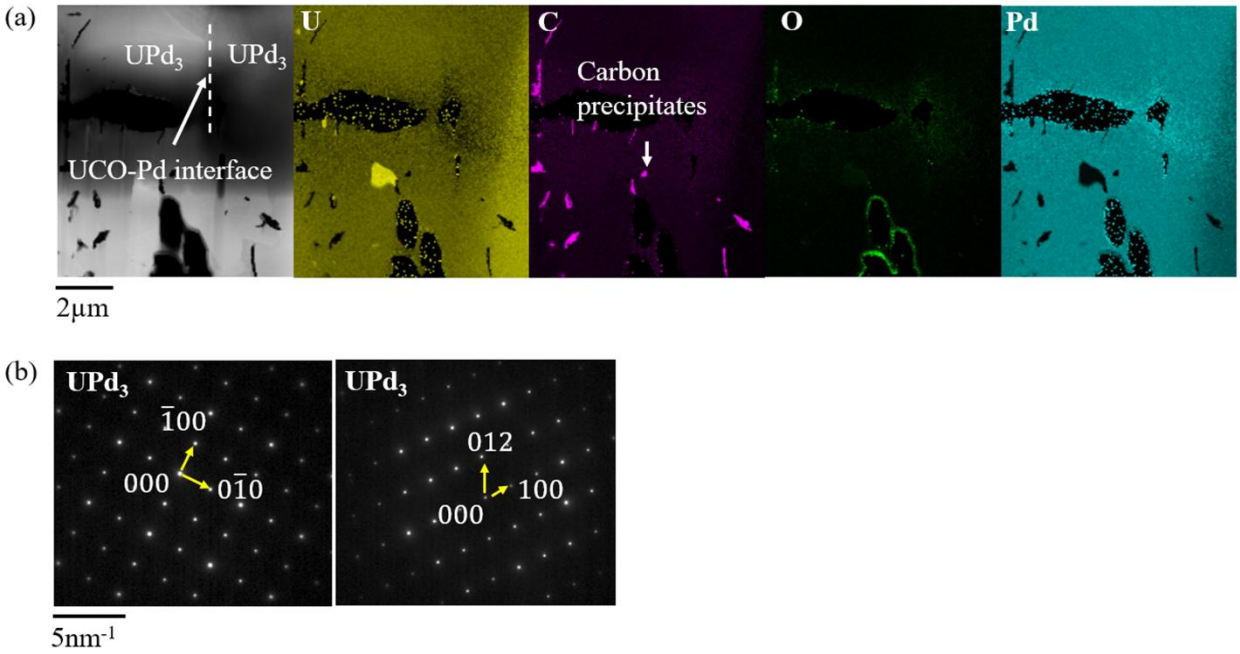


Figure 3. STEM EDS and SAED patterns collected at the interface region. (a) STEM-EDS maps (b) SAED patterns. STEM-EDS reveals that Pd was present throughout the lift-out at the interface and carbon precipitates were present. SAED patterns confirm the formation of hexagonal UPd_3 phase on either side of the interface.

Figure 4 shows STEM-EDS and SAED patterns of lamellar structure (4a-4b) and equiaxed region (4c-4d) at the Pd interaction zone, respectively. Both microstructures exhibited UPd_3 formation; however, unlike at the interface, prominent UC and UO_2 phases were still present. The presence of all three phases—UC, UO_2, and UPd_3—were confirmed at both locations. SAED patterns were consistent with the crystal structures of cubic fluorite UO_2, cubic rock salt UC, and hexagonal UPd_3. STEM-EDS and SAED analysis in this work revealed UPd_3 as a reaction product after chemical interactions between Pd and UCO. We studied phase evolutions in U-C-Pd system using isothermal ternary phase diagrams at 1100 ºC and room temperature (RT) as shown in Figures 5c and 5d. The RT diagrams are to showcase that the UPd_3 remains stable even when

sample temperature was ramped down for cooling. The results confirm the formation of UPd_3 even with slight addition of Pd.

The fuel kernel consists of a combination of UC, U_2C_3, and UO_2 phases, each exhibiting distinct FP interaction mechanisms. UO_2 is known for its chemical stability, with the primary concern being gas release[13]. It is likely that only UC and U_2C_3 phases may have reacted with Pd. In the case of this UCO-Pd diffusion couple, no other oxide phases were observed other than UO_2. The possible reactions between Pd, UO_2, UC, and U_2C_3 phases are shown in reactions (1), (2), and (3), respectively. Gibbs free energy of reaction ΔG_{rxn} versus temperature plot obtained using HSC Chemistry software [32] in Figure 6 also confirm positive ΔG_{rxn} for reaction (1), which means the reaction between Pd and UO_2 is not spontaneous. ΔG_{rxn} versus temperature plot in Figure 6 revealed consistently negative ΔG for both reaction (2) and (3) suggesting spontaneous reactions between Pd and UC, and Pd and U_2C_3 phases could occur at any temperature ranging from 25 °C to 1200 °C.

$$UO_2 + 3Pd \rightarrow UPd_3 + O_2 \quad (1)$$

$$UC + 3Pd \rightarrow UPd_3 + C \quad (2)$$

$$U_2C_3 + 6Pd \rightarrow 2UPd_3 + 3C \quad (3)$$

The presence of UC and carbon discontinuous precipitates at the grain boundaries and U_2C_3 intragranular string precipitates shown in Figure 1b reveals the apparent degradation of UC during annealing. The absence of Pd in the annealed UCO zone only allowed for thermally driven microstructural changes to occur but perfectly illustrated that UC degrades in these conditions and hence be more reactive with Pd. Moreover, Figures 3, 4a, and 4c are lamellae extracted from the

Pd interaction zone: at the interface, lamellar region, and equiaxed region respectively. These lamellae show evidence of degradation of UC due to the presence of high carbon precipitates distributed across the lamellae.

The formation of different microstructures can be attributed to the Pd reaction site. If the Pd reaction site is the intragranular U_2C_3 string, it may result in the formation of an alternating UC and UPd_3 structure, which appears as a lamellar microstructure. Similarly, carbon discontinuous precipitates at the grain boundary can also serve as Pd reaction sites, potentially leading to the formation of rounder, equiaxed grains. As these new phases nucleate, uranium from the surrounding UC matrix is consumed, leaving behind vacancy clusters that naturally coalesce into pores. Concurrently, as carbon precipitates form across the matrix, it causes carbon depletion that destabilizes the carbide structure and promotes additional pore formation as the weakened lattice collapses[9,33].

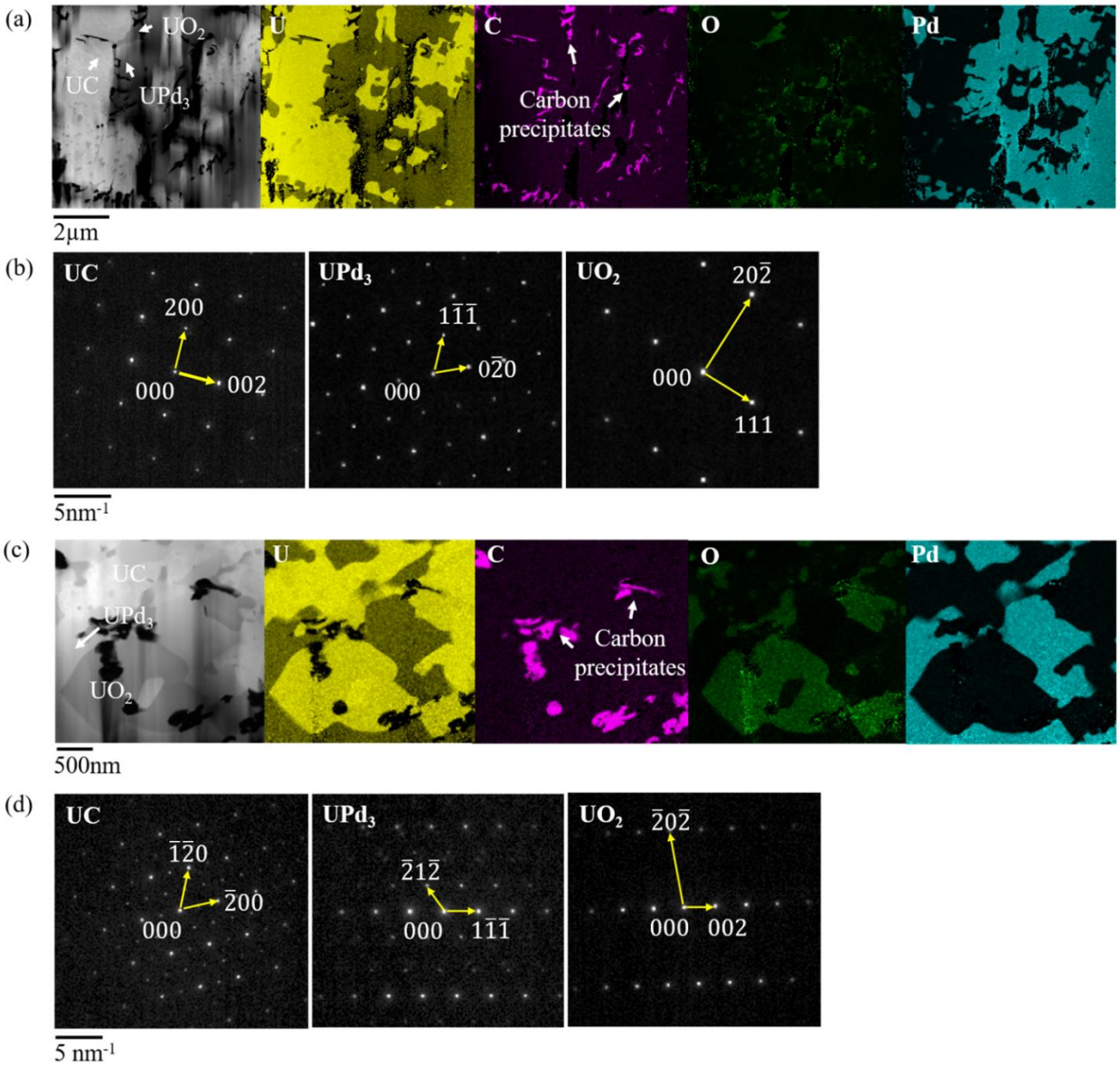


Figure 4. STEM EDS maps and diffraction patterns collected from lamellar structure (a-b) and equiaxed grain (c-d) at the Pd interaction zone. Both confirm the presence of all three phases: UC, UO_2, and UPd_3.

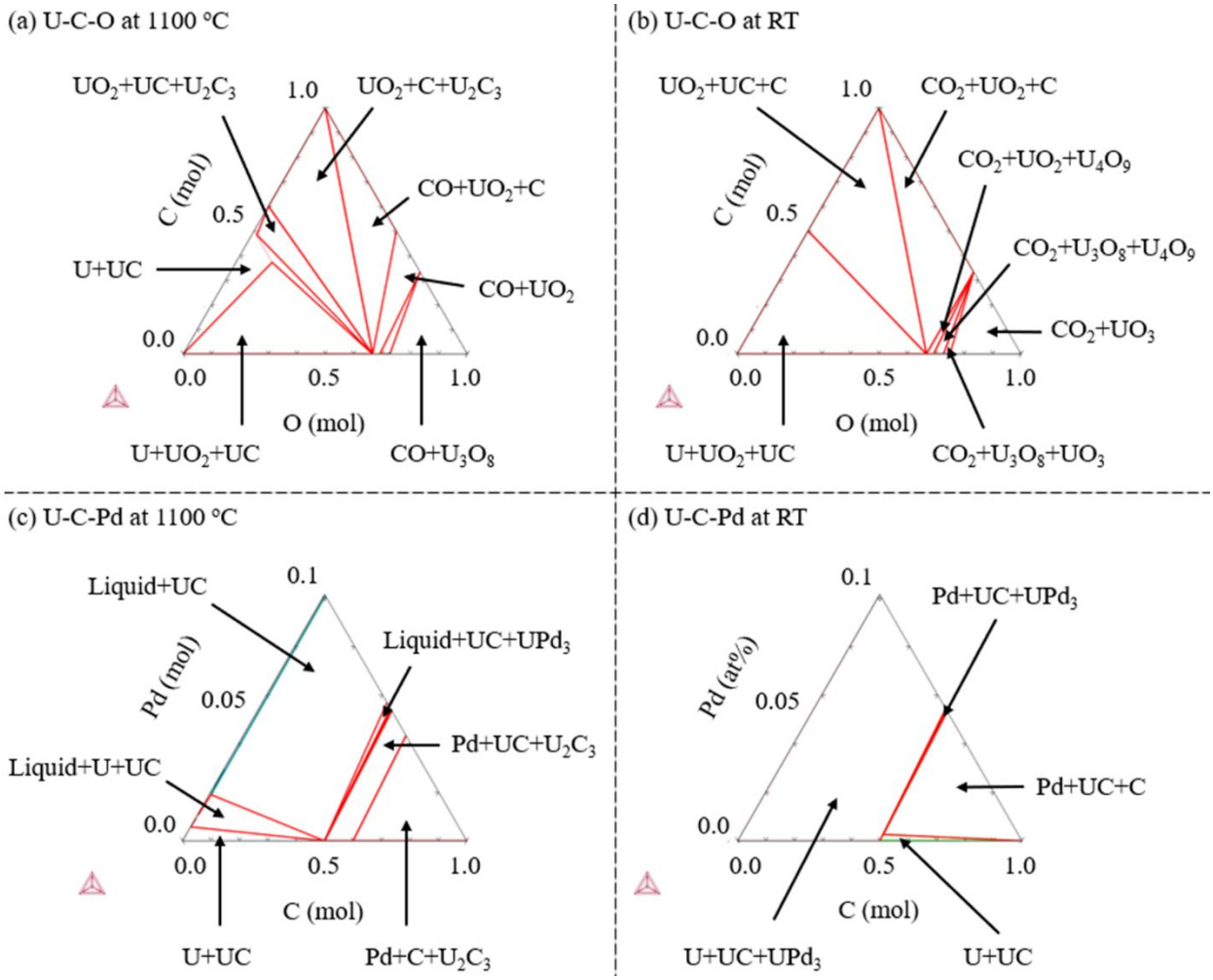


Figure 5. **Isothermal ternary phase diagrams of U-C-O system generated using ThermoCalc at:** (a) 1100 ºC and (b) RT, and U-C-Pd system at (c) 1100ºC and (d) RT.

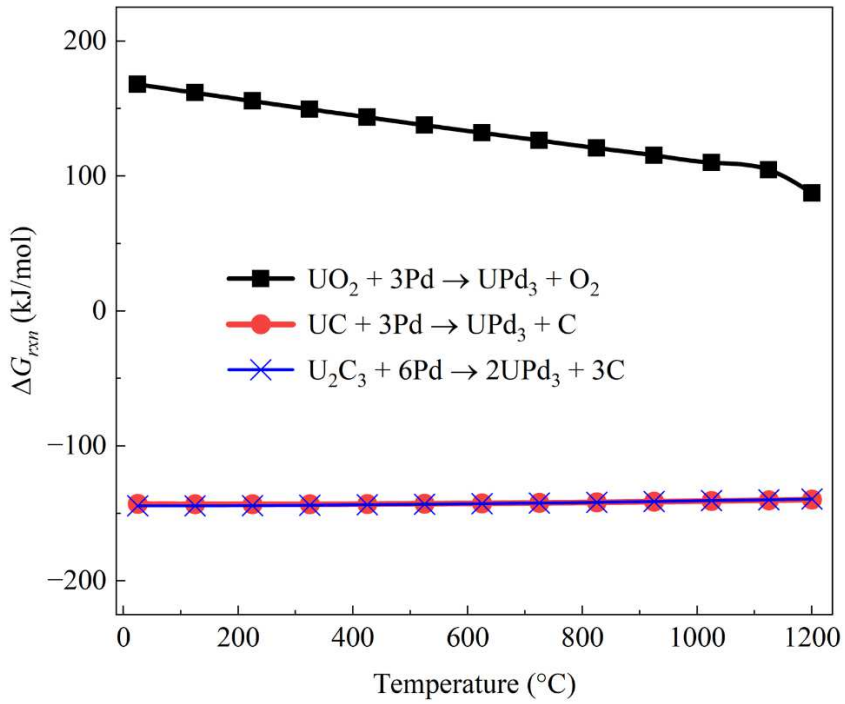


Figure 6. Gibbs free energy of reaction (ΔG_{rxn}) as a function of temperature for Pd chemical interactions with UO_2, UC and U_2C_3 phases. Plot shows negative ΔG_{rxn} indicating spontaneity for Pd reactions with UC and U_2C_3, while plot shows positive ΔG_{rxn} indicating non-spontaneity for Pd reaction for UO_2.

2.3. Mechanical properties after Pd diffusion

The interaction between UCO and Pd facilitated the formation of Pd-containing intermetallic phases, as previously identified via TEM analysis. The nucleation and growth of these precipitates, along with the development of altered grain boundary structures, are anticipated to significantly influence the mechanical properties of the fuel, with potential implications for its in-reactor performance. Mechanical property characterization was performed using nanoindentation

techniques to evaluate and compare the hardness profiles of the annealed UCO zone and the Pd interaction zone. A quantitative heat map was generated to depict the phase-specific hardness distribution, as illustrated in Figure 7. Regions of elevated hardness, represented by green to red gradients, corresponded to the UC phase, while intermediate hardness values, shown in light blue to green, were associated with the UO_2 phase. The lowest hardness values, depicted in dark blue, were attributed to the UPd_3 phase.

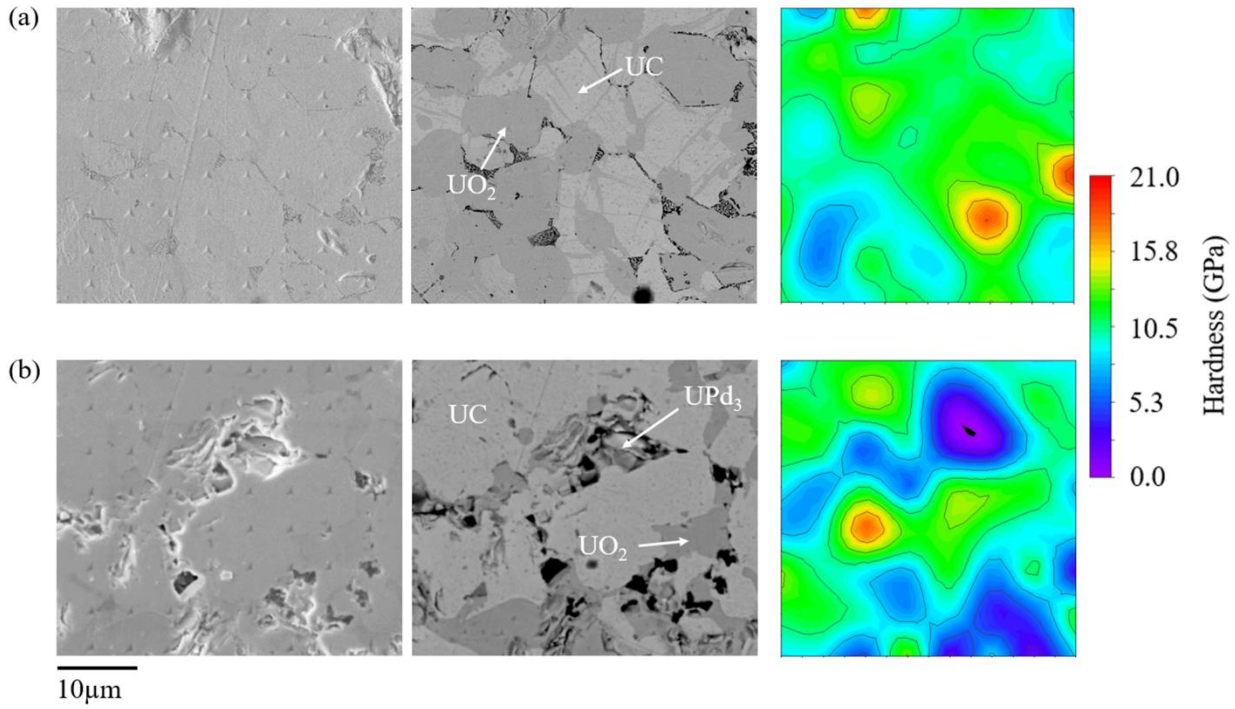


Figure 7. Nanoindentation SEM images and heat map representing varying hardness measurements across annealed UCO and Pd interaction zone. (a) L-R SEM images of nanoindentation marks on the annealed UCO zone, BSE-SEM image showing the contrast of color between lighter color UC and darker color UO_2, heat map summarizing hardness (GPa) in annealed UCO region; (b) L-R SEM images of nanoindentation marks in interaction zone where Pd diffused, heat map summarizing hardness (GPa) in interaction region.

Nanoindentation data, presented in Figure 8, revealed significant variability in hardness within the interaction zone, alongside a pronounced reduction in mean hardness, which is attributed to Pd phase evolution. In contrast, the annealed UCO zone exhibited minimal variability and maintained a relatively uniform mechanical response. Specifically, the UCO annealed zone displayed a mean hardness of 10.86 GPa, whereas the Pd interaction zone exhibited a reduced mean hardness of 9.05 GPa.

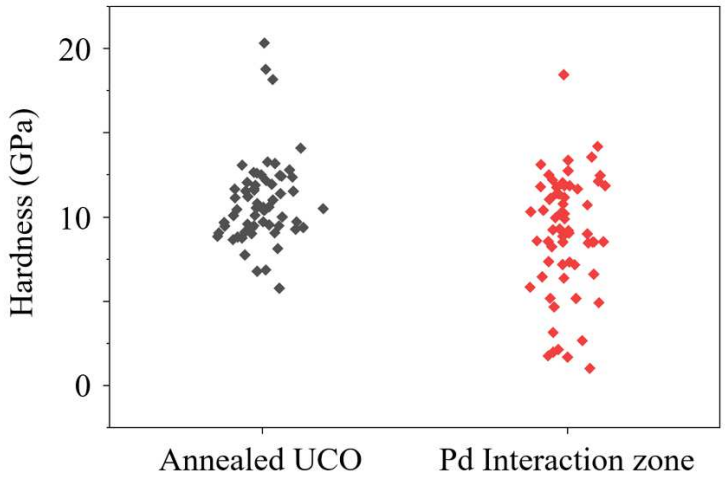


Figure 8. Scatter plot represents hardness distribution in Pd interaction zone and annealed UCO zone. Due to surface voids and roughness, the Pd interaction zone tends to exhibit greater variability in hardness compared to the annealed UCO zone.

The presence of metallic precipitates is said to contribute to grain boundary embrittlement, act as localized stress concentrators, and promote intergranular cracking[34,35]. In Figure 8, the hardness data within the Pd interaction zone exhibits significantly greater scatter compared to the annealed UCO zone. This variability is attributed to the presence of Pd phases, which have induced the formation of pores and increased surface roughness in the Pd interaction zone. Nanoindentation in

Pd interaction zone often landed on pore-rich areas, yielding lower hardness values, while other tests probed UO_2 or UPd_3, both of which have lower hardness than UC. Additionally, the increased surface roughness prevented full contact between the indenter tip and the material surface, further contributing to reduced hardness readings. To refine these findings, additional mechanical testing is recommended to gather a more comprehensive dataset that accurately quantifies the hardness of UC, UO_2, and UPd_3 phases individually. Given the small size and scattered distribution of UPd_3 phases, it would be beneficial to pair mechanical testing with imaging techniques, such as electron microscopy, to enable precise targeting of specific regions of interest. This approach would enhance the accuracy and reliability of future measurements. The team is in the process of designing a mechanical characterization involving SEM in-situ micro tensile testing.

This paper investigated the effect of Pd fission product on microstructure and mechanical properties of UCO nuclear fuel. The degradation of UCO fuel is evidenced by the formation of grain boundary carbon precipitates and intragranular U_2C_3 string precipitates after annealing and intermetallic UPd_3 phase after Pd diffusion. The presence of UPd_3, carbon precipitates, and porosity at the interfacial region between UCO-Pd diffusion couple clearly decreased the mechanical properties. Although the UCO-Pd diffusion couple used in this study does not fully replicate the scale or distribution of Pd fission products in irradiated UCO fuel, it nevertheless provides essential insight into Pd transport and high-temperature degradation mechanisms. The experimental configuration introduces a larger, continuous Pd source than would exist in-reactor, this controlled interface enables direct observation of Pd diffusion pathways, reaction products, and phase evolution that are difficult to resolve from irradiated samples alone. Thus, while the diffusion-couple geometry does not fully replicate the spatial distribution of fission-product Pd in-reactor, these findings even if geometry is not perfectly representative of true fission-product

behavior, these findings meaningfully enhance our understanding of Pd mobility in UCO and inform interpretation of degradation mechanisms in UCO fuel exposed to elevated temperatures.

3. Methods

3.1. Diffusion experiments

The diffusion couple consisted of UCO fuel kernel obtained from Ultra Safe Nuclear Corporation lot # USNC-UCO-230215-CF, and a commercially available 99.99% purity Pd foil from Alfa Aesar. Diffusion couple assembly was prepared in an argon environment with pH_2O and pO_2 levels ≤ 1ppm[36]. The assembly underwent annealing in a Carbolite Geo high temperature horizontal tube furnace at 1100 °C held for 100 hours maintained in an argon environment as shown in the schematic in Figure 9a. High-temperature annealing drives faster Pd diffusion and subsequent reaction with UCO fuel. Preliminary low-magnification EDS analysis (Figure 9b) shows both the annealed UCO region distant from the Pd foil and the Pd interaction zone at the UCO–Pd interface.

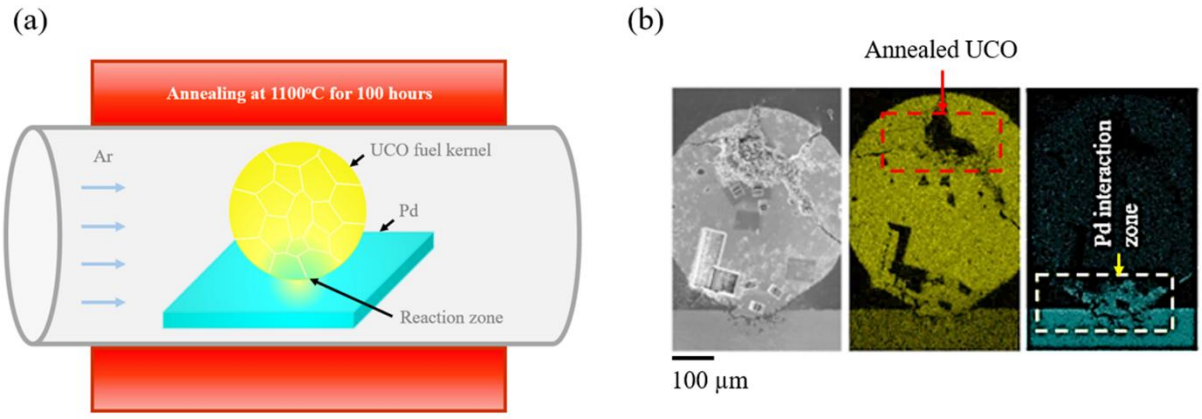


Figure 9. Diffusion couple consist of UCO kernel and Pd bar was annealed in a furnace at 1100°C for 100 hours. (a) Schematic diagram illustrating UCO-Pd diffusion couple and annealing in a tube furnace at 1100°C, (b) preliminary SEM-EDS mapping of UCO-Pd diffusion couple.

3.2. Microstructure and mechanical characterizations

Microstructural and mechanical characterizations were performed at Idaho National Laboratory's Microscopy and Characterization Suite (MaCS). SEM imaging and EDS mapping were performed using a JEOL 6610 scanning electron microscope with beam conditions 20kV and 60 spot size. Several lift-outs were prepared from the diffusion couple using an in-situ lamella extraction with a Thermo Scientific Quanta 3D FEG dual-beam system. The extraction used beam settings ranging from 30 kV at 10 pA up to 15 nA, followed by a 5 kV, 48 pA cleaning step to minimize gallium-induced damage. A lift-out from the unannealed 'pristine UCO' sample was also extracted to serve as a baseline. For the annealed sample, lift-outs were extracted from annealed UCO and different regions within Pd interaction zone. All lift-outs were mounted onto copper TEM half-grids and were thinned to electron transparency using the ion beam. These lamellae were examined using a Thermo Scientific Spectra 300 STEM equipped with Super X

EDS. We examined phase evolution in the U–C–O system using Thermocalc 2026a isothermal ternary phase diagrams at 1100 °C and room temperature. TAF-ID fuels database was used without suppressing any phases. Atmospheric pressures were used for calculations. Lastly, a series of 8×8 hardness tests were performed on both the UCO-annealed region and the Pd interaction zone using a Hysitron TI-95 TriboIndenter. The measurements used a standard load configuration with a Berkovich nanoindenter tip, applying a maximum load of 12.5 mN and a spacing of 5 μm.

Data availability statement

The digital data for all figures, tables, charts, and any other media contained in this publication will be made available on request.

Competing interests

The authors declare that they have no financial or non-financial competing interests.

Authors' contributions

JH: Conceptualization, Investigation, Methodology, Writing – original draft preparation. **KB:** Conceptualization, Supervision, Investigation, Methodology, Writing – original draft preparation. Writing – review and editing**. JL:** Investigation, Methodology, Writing – review and editing. **AK:** Investigation, Methodology, Writing – review and editing. **CS –** TEM data acquisition. **GY** – TEM data acquisition. **SC-** Investigation, Methodology. **PW** Supervision, Funding acquisition, Writing – review and editing. **TY:** Supervision, Funding acquisition, Writing

– review and editing. **ES** Supervision, Funding acquisition, Project administration, Writing – review and editing. **HZ** Supervision, Investigation- data analysis and mechanism development, Writing – review and editing. All authors read and approved of the final manuscript.

Acknowledgments

This work was supported as a part of the Integrated Research Projects program, funded by the US Department of Energy, Office of Nuclear Energy (DOE-NE). The authors also acknowledge the U.S. DOE-NE under DOE Idaho Operations Office Contract DE-AC07-051D14517, for use of the resources as part of Nuclear Science User Facilities. The authors thank Dr. Mukesh Bachhav, Mr. Jeremy Burgener, and Ms. Kristi Moser-McIntire for their support as this work transpired in Critical Materials and Energy Systems Innovation Center (CMESIC).

References

1. Minato, K. & Ogawa, T. advanced concepts in TRISO Fuel. in *Comprehensive Nuclear Materials (Second Edition)* (eds Konings, R. J. M. & Stoller, R. E.) 334–360 (Elsevier, Oxford, 2020).
2. Nuclear Fuels. *Energy.gov* https://www.energy.gov/ne/nuclear-fuels.
3. Geelhood, K. J. PNNL-31427 - TRISO Fuel: properties and failure modes.
4. Lowe, T. *et al.* Microstructural analysis of TRISO particles using multi-scale x-ray computed tomography. *J. Nucl. Mater.* **461**, 29–36 (2015).
5. Demkowicz, P. A., Liu, B. & Hunn, J. D. Coated particle fuel: historical perspectives and current progress. *J. Nucl. Mater.* **515**, 434–450 (2019).

6. Rohbeck, N. & Xiao, P. Evaluation of the mechanical performance of silicon carbide in TRISO fuel at high temperatures. *Nucl. Eng. Des.* **306**, 52–58 (2016).
7. Peng, L., Yang, Y., Li, S., Nong, Z. & Tang, S. Investigation on irradiated-thermal-mechanical coupling performance and failure behaviors of TRISO particle fuel for space reactor applications. *Prog. Nucl. Energy* **180**, 105633 (2025).
8. Seibert, R. L., Jolly, B. C., Balooch, M., Schappel, D. P. & Terrani, K. A. Production and characterization of TRISO fuel particles with multilayered SiC. *J. Nucl. Mater.* **515**, 215–226 (2019).
9. Njifon, I. C. & Torres, E. Carbon driven oxygen retention in uranium oxycarbide (UCO) fluorite phase. *J. Nucl. Mater.* **563**, 153662 (2022).
10. Liu, X.-Y. *et al.* Atomistic and cluster dynamics modeling of fission gas (Xe) diffusivity in TRISO fuel kernels. *J. Nucl. Mater.* **561**, 153539 (2022).
11. Bawane, K. *et al. In-Situ* TEM study of microstructural evolution in proton irradiated single crystal UO2 under high-temperature annealing. *Acta Mater.* **281**, 120440 (2024).
12. Cheik Njifon, I. & Torres, E. Atomistic investigation of uranium oxycarbide (UCO) phase stability at finite temperatures: DFT+U and AIMD+U U approaches. *J. Nucl. Mater.* **554**, 153046 (2021).
13. Lyons, M. F., Boyle, R. F., Davies, J. H., Hazel, V. E. & Rowland, T. C. UO_2 properties affecting performance. *Nucl. Eng. Des.* **21**, 167–199 (1972).
14. Clark, R. A. *et al.* Distribution of metallic fission-product particles in the cladding liner of spent nuclear fuel. *Npj Mater. Degrad.* **4**, 4 (2020).
15. Parrish, R. J. *et al.* Characterization of solid fission products in 13.7% FIMA MOX fuel using electron microscopy techniques. *J. Nucl. Mater.* **524**, 67–79 (2019).

16. Sato, I., Furuya, H., Arima, T., Idemitsu, K. & Yamamoto, K. Behavior of metallic fission products in uranium–plutonium mixed oxide fuel. *J. Nucl. Mater.* **273**, 239–247 (1999).
17. Wen, H. & van Rooyen, I. J. Distribution of fission products palladium, silver, cerium and cesium in the un-corroded areas of the locally corroded SiC layer of a neutron irradiated TRISO fuel particle. *J. Eur. Ceram. Soc.* **37**, 3271–3284 (2017).
18. Bleam, W. Chapter 1 - Element Abundance. in *Soil and Environmental Chemistry (Second Edition)* (ed. Bleam, W.) 1–38 (Academic Press, 2017).
19. Minato, K. *et al.* Fission product palladium-silicon carbide interaction in htgr fuel particles. *J. Nucl. Mater.* **172**, 184–196 (1990).
20. Cavazos, S. J. *et al.* Palladium corrosion of the SiC layer in TRISO particle fuels: a separate effects study to assess mechanisms for palladium attack. SSRN Scholarly Paper at https://doi.org/10.2139/ssrn.5384686 (2025).
21. Lillo, T. M. & van Rooyen, I. J. Associations of Pd, U and Ag in the SiC layer of neutron-irradiated TRISO fuel. *J. Nucl. Mater.* **460**, 97–106 (2015).
22. Tiegs, T. N. Fission product Pd-SiC interaction in irradiated coated-particle fuels. **57**, 389–398 (1982).
23. Devaraj, A. *et al.* Phase transformation of metastable discontinuous precipitation products to equilibrium phases in U10Mo alloys. *Scr. Mater.* **156**, 70–74 (2018).
24. Han, W., Gao, J., Li, M., Zhang, M. & Liu, R. Impact of fission product (Ce, Sn, Sr, Se) oxides on UO2 oxidation to U3O8. *Prog. Nucl. Energy* **171**, 105194 (2024).
25. Jana, S. *et al.* Kinetics of cellular transformation and competing precipitation mechanisms during sub-eutectoid annealing of U10Mo alloys. *J. Alloys Compd.* **723**, 757–771 (2017).

26. Althaus, W., Cook, M. & Bieker, R. A study of as - cast and heat - treated uranium - uranium carbide alloys by optical and electron microscopy. AFC Research and Development Report (1966).

27. Kamboj, A., Perry, N. & Marquis, E. A. Mechanisms of phase decomposition in a non-equimolar CrFeMnNi alloy during thermal aging. *Materialia* **36**, 102146 (2024).

28. Fang, J. Y. C. *et al.* Competition between continuous and discontinuous precipitation in L12-strengthened high-entropy alloys. *Intermetallics* **149**, 107655 (2022).

29. Benz, R. & Farr, J. D. X-ray diffraction of UC-UC_2 and UC-UN alloys at elevated temperatures. *J. Nucl. Mater.* **42**, 217–222 (1972).

30. Ol, N. phase transformation of hyper stoichiometric uranium carbide. Atomic Energy of Canada. (1970).

31. Kurasawa, T., Watanabe, H. & Kikuchi, T. Transformation to U_2C_3 phase in UC-UC_2 and UC_2 phases. *J. Nucl. Mater.* **43**, 192–204 (1972).

32. Roine, A. HSC Chemistry. (2023).

33. Kindall, E. C. *et al.* Thermal oxidation and high temperature structural behavior of uranium carbide. *Npj Mater. Degrad.* **10**, 19 (2026).

34. Liang, R.-T. *et al.* Effects of fission product doping on the structure, electronic structure, mechanical and thermodynamic properties of uranium monocarbide: A first-principles study. *Nucl. Eng. Technol.* **55**, 2556–2566 (2023).

35. Athon, M. T. *et al.* Quantitative morphological characterization of carbide inclusions in uranium metal. *J. Nucl. Mater.* **558**, 153370 (2022).

36. Cavazos, S. mass transport of metallic fission products in advanced particle fuels Ph. D. dissertation. (2024).

Supplementary Files

This is a list of supplementary files associated with this preprint. Click to download.

- SupplementaryInformation.pdf